

# An effective phase field method for topology optimization without the curvature effects

Wenxuan Xie, Qing Xia, Qian Yu, Yibao Li \*

School of Mathematics and Statistics, Xi'an Jiaotong University, Xi'an 710049, China

## ARTICLE INFO

### Keywords:

Topology optimization  
Phase field method  
Curvature effect  
Preconditioning process

## ABSTRACT

In this paper, we will present a novel phase field based topology optimization method without the curvature effects. The original phase field based topology optimization method greatly simplifies gridding, discretization, and handling of topological changes. However, the interface motion driven by curvature effects exists in the original phase field equation, which significantly affects the performance of structure. Furthermore, the existence of curvature effects also bring the ill-conditioned behavior of the normal vector. To overcome these shortcomings, we propose a modified phase field method with a nonlinear preconditioning process to eliminate the curvature effects. The method performs interface corrections on topological shapes through an anti-diffusive phase-field equation and imposes an adaptive preconditioning process to alleviate the problems of erroneous normal vector. The adaptive preconditioning method can capture more shape details for traditional topology optimization methods and offset the over-smooth effect of the phase field framework. We couple the finite element method and the finite difference method to solve the compliance minimization problem. The linearly stabilized splitting scheme is adopted to maintain the simplicity and stability of the algorithm. A series of comparative numerical examples are performed to show the feasibility and effectiveness of the proposed method. These examples demonstrate the superiority of our method compared to the original phase field method for topology optimization.

## 1. Introduction

Topology optimization [1–5] focuses on seeking the optimum distribution of material in a design domain that minimizes a objective function under a series of constraints. The importance of topology optimization lies in the fact that the selection of the appropriate structural topology at the conceptual stage will usually determine the efficiency of a new product. As an effective mechanical design tool in larger industries and academia, topology optimization has increased tremendously in popularity [6], which plays an important role in compliance problem [7,8], heat transfer problems [9], viscoelastic structure design [10] and multiscale design in solid mechanics [11]. Due to the wide application of topology optimization, the numerical methods for such issue have received considerable attention.

Numerical methods for continuum structural topology optimization have been extensively investigated and developed. Among these numerical methods, density-based method is widely used. Such method introduces element-wise material density variables and steers them to-

wards a discrete solid/void solution by using material interpolation schemes, such as the homogenization methods [3,12], evolutionary structural optimization (ESO) method [13], rational approximation of material properties (RAMP) method [14] and solid isotropic material with penalization (SIMP) method [15]. Density-based methods hold the advantages of simplicity and ease of use, however, these methods tend to suffer from numerical instabilities including non-physical checkerboard patterns, grayscales and mesh dependency [16]. Additional correction techniques need to be introduced to correct these instabilities such as sensitivity or density filtering techniques [17].

In order to obtain clear shapes from the optimal density distribution without the use of filtering methods, boundary variation method is proposed. This type of approach uses the structure boundary as a design variable and represents the structure boundary implicitly. The level set method and phase field method are two representative boundary variation methods [18–22]. For the level set method, structural boundaries can be implicitly defined by a zero contour of the level set function and Hamilton-Jacobi equation is used to evolve level set function. Orig-

\* Corresponding author.

E-mail address: [yibaoli@xjtu.edu.cn](mailto:yibaoli@xjtu.edu.cn) (Y. Li).

URL: <http://gr.xjtu.edu.cn/web/yibaoli> (Y. Li).

<https://doi.org/10.1016/j.camwa.2023.06.037>

Received 27 October 2022; Received in revised form 12 May 2023; Accepted 29 June 2023

inally introduced by Osher and Sethian [23], it has been applied in many research fields such as fluid mechanics and image processing. The seminal work incorporating level set method into structural optimization can be found in [24]. To maintain sufficient numerical accuracy, the level set function needs to be re-initialized during the update operation to maintain the signed distance function characteristic [25]. A number of approaches concerned about re-initialization operation have been proposed in [26,27]. Moreover, it is difficult for the level set method to satisfy the volume conservation due to re-initialization error and conservation error [28]. Research applying the phase field method to practical physical models can be traced back to Cahn and Hilliard [29] and Allen and Cahn [30]. Now this method has been applied in solid-liquid transitions [31], crystal growth [32,33], crack-propagation [34], image segmentation [35]. The phase field method is capable of tracing the boundary motion which couples state variables such as temperature or the displacement in elasticity. This method introduces a phase-field function to describe the phase transition, this function varies smoothly in the single-phase region, but sharply across the diffused interface region [28]. The mathematical formulation of applying phase field method to structural optimization was given by Bourdin and Chambolle [36,37]. Allen-Cahn equation was successfully applied to topology optimization by Takezawa et al. [25]. Later Wallin and Ristinmaa [38] applied the Takezawa model to the minimum compliance problem under a constant-volume problem.

Although the phase field method has been widely applied in topology optimization because of its flexibility and simplicity, the following issues still need to be addressed. When the conventional phase field method is employed in topology optimization, a target to reduce the interface perimeter is added to the objective function. The introduction of such a target is caused by the curvature driving of the interface migration due to the presence of Laplacian operator in the phase field equation [39]. However, there is no curvature-driven interface motion in the original objective function, thus the curvature effect should be eliminated from the phase field evolution equation. Modified Allen-Cahn equations that remove the curvature effect from the original Allen-Cahn equation are proposed [28,40,41]. It is a remarkable fact that the modified method can keep more details of the structure topology during the evolution, but a challenging problem which arises in the modified method is the ill-conditioned behavior of the normal vector. The main reason for this phenomenon is the numerical errors caused by approximation of unit normal vector. The similar issue is observed in the conservative level-set method. The idea of nonlinear preconditioning for normal vector correction recycles the signed distance function using inverse hyperbolic tangent, and can improve the accuracy of normal computations [42]. Based on the normal vector correction method, Chiu [43] proposed a nonlinear preconditioning phase field equation to solve the two-phase incompressible flows. Jabir et al. [44] developed an alternative preconditioning method based on traditional level-set re-initialization which minimizes interface displacement. It is heuristic to solve the topology optimization problem by performing interface corrections on topological shapes to track the sharp interface accurately and effectively.

In this paper, we will develop a modified phase field method with a nonlinear preconditioning process to solve topology optimization problems. In order to seek the optimal distribution of material in a design domain, we derive the phase field evolution equation based on the conservative Allen-Cahn equation [7]. In present work, we use the modified equations that remove the curvature effect in the different contexts and applications. An anti-diffusive phase-field equation is established. In this way, the curvature effects is omitted from the original phase field evolution equation, which can ensure that the purpose of minimizing the objective function is not interfered by curvature effects. To our knowledge, the presented approach is the first algorithm applying such a correction method for topology optimization problems. The issues of numerical oscillation and the ill-conditioned behavior of the normal vector during evolution can be avoided due to the existence of

preconditioning process. Finite element method is utilized to calculate the linear elasticity equation, and finite difference scheme is applied to both modified phase field equation and preconditioning process. In order to improve the stability of our schemes, the linearly stabilized splitting method is adopted, a semi-implicit scheme is used to discretize the original phase field equation. Meanwhile explicit scheme is applied to the modified term and preconditioning equation, which implies that our scheme is stable and efficient. We carry out a series of comparative experiments to verify the effect of the proposed model.

This paper is organized as follows. In Section 2, we describe the original problem with phase field method and the present modified phase field method with preconditioning process. In Section 3, we describe the numerical scheme. Numerical experiments and results are performed in Section 4. Some conclusions are presented in Section 5.

## 2. Model formulation

### 2.1. Original problem with phase field method

Let us consider  $\Omega \subset R^2$  as the design domain divided into two sub-regions  $\Omega_0$  and  $\Omega_1$ , which represents void domain and solid domain. The boundary area between two phases  $\Omega \setminus (\Omega_0 \cup \Omega_1)$  is called the interface diffuse region, which usually holds the thickness  $\epsilon$ . The phase field function  $\phi(\mathbf{x})$  is applied to represent the state of two phases at each local point  $\mathbf{x}$  in  $\Omega$ , which can be defined as  $\phi(\mathbf{x}) = 1$  in  $\Omega_1$ ,  $\phi(\mathbf{x}) = 0$  in  $\Omega_0$  and  $0 < \phi(\mathbf{x}) < 1$  in  $\Omega \setminus (\Omega_0 \cup \Omega_1)$ .

Next we discuss the compliance minimization problem, which is a classic example in topology optimization problem. The objective function and the constraints are established as:

$$\begin{aligned} \min : \quad & J(\phi) = \int_{\Omega} W(\phi) d\mathbf{x}, \\ \text{subject to : } & \nabla \cdot \sigma(\phi, \mathbf{u}) = \nabla \cdot g(\phi) \sigma^0 = \mathbf{0}, \text{ in } \Omega, \\ & V(\phi) = \int_{\Omega} \phi d\mathbf{x} = V_0, \\ & 0 \leq \phi \leq 1. \end{aligned} \quad (1)$$

Here,  $\mathbf{u} = (u, v)$  is displacements with  $x$ -component  $u$  and  $y$ -component  $v$ ,  $V_0$  is constrained volume fraction and  $W(\phi) = (\epsilon(\mathbf{u}) : \mathbf{D}(\phi) : \epsilon(\mathbf{u})) / 2$  represents local elastic strain energy density. The operator: is the sign of tensor inner product. Meanwhile,  $\epsilon(\mathbf{u})$  and  $\sigma^0$  are second-order tensors represent the strain tensor and stress tensor respectively,  $\sigma = g(\phi) \sigma^0$  is a second-order tensor coupling interpolation function  $g(\phi)$  and stress tensor  $\sigma^0$ , where we introduce a two-point interpolation function  $g(\phi) = g_{min} + (1 - g_{min}) \phi^3$  in order to avoid singularity problem caused by the zero value of  $\phi$  in calculation,  $g_{min}$  is a small positive value. Specifically, with the definition of  $g(\phi)$ , the distribution of  $\sigma$  in entire domain can be expressed as follows:

$$\sigma = \begin{cases} g_{min} \sigma^0 & \mathbf{x} \in \Omega_0, \\ g(\phi) \sigma^0 \quad (g_{min} \leq g(\phi) \leq 1) & \mathbf{x} \in \Omega \setminus (\Omega_0 \cup \Omega_1), \\ \sigma^0 & \mathbf{x} \in \Omega_1. \end{cases}$$

Furthermore,  $\mathbf{D}(\phi) = g(\phi) \mathbf{D}^0$  is the virtual stiffness tensor coupling interpolation function  $g(\phi)$  and fourth-order stiffness tensor  $\mathbf{D}^0$ , the formulation of  $\mathbf{D}^0$  is expressed as:

$$D_{ijkl}^0 = 2G \left( \delta_{ik} \delta_{jl} + \frac{\nu}{1-2\nu} \delta_{ij} \delta_{kl} \right),$$

where  $G = E / (2(1 + \nu))$  is the shear modulus,  $E$  is the elasticity modulus,  $\nu$  is poisson ratio,  $\delta$  is Dirichlet function. The fourth-order tensor  $\mathbf{D}^0$  is used to represent a solid's stiffness, which established the relationship between increments of stress and increments of strain. For the establishment of  $\mathbf{D}^0$ , please refer to [45,46]. In elastostatics, equilibrium equation, constitutive equation and strain-displacement equation

are used to characterize the coupling relationship of  $\mathbf{u}$ ,  $\varepsilon$  and  $\sigma^0$  in design domain  $\Omega$ :

$$\begin{cases} \nabla \cdot \sigma^0 = \mathbf{0}, \\ \sigma^0 = \mathbf{D}^0 : \varepsilon(\mathbf{u}), \\ \varepsilon(\mathbf{u}) = \frac{1}{2} (\nabla \mathbf{u} + (\nabla \mathbf{u})^T). \end{cases} \quad (2)$$

Displacement variable  $\mathbf{u}$  need to be solved by Eq. (2) with specific boundary conditions using finite element method [6,47,48]. There are two boundary conditions in the study of linear elasticity, displacement boundary condition  $\mathbf{u} = \mathbf{u}_D$ , and stress boundary condition  $\mathbf{n} \cdot \sigma^0 = \mathbf{s}$ . Here  $\mathbf{u}_D$  is the determine boundary displacement,  $\mathbf{s}$  is traction boundary forces and  $\mathbf{n}$  is the outward norm vector on boundary. We will consider the mixed boundary condition consisting of the zero displacement boundary condition and stress boundary condition in this paper, the equilibrium equation is

$$\nabla \cdot \sigma(\phi, \mathbf{u}) = \mathbf{0}, \quad (3)$$

$$\begin{cases} \mathbf{u} = \mathbf{0}, & \text{on } \Gamma_1 \subset \partial\Omega, \\ \mathbf{n} \cdot \sigma(\phi, \mathbf{u}) = \mathbf{s}, & \text{on } \Gamma_2 \subset \partial\Omega, \\ \mathbf{n} \cdot \sigma(\phi, \mathbf{u}) = \mathbf{0}, & \text{on } \partial\Omega / (\Gamma_1 \cup \Gamma_2). \end{cases} \quad (4)$$

In this paper, we first give the original phase field evolution equation by minimize the modified energy [7], the energy function contains the Ginzburg-Landau free energy, the principle of virtual work and the volume constraint can be constructed as follows:

$$E(\phi, \mathbf{u}) = \eta \int_{\Omega} W(\phi, \mathbf{u}) d\mathbf{x} + \frac{\beta}{2} (V(\phi) - V_0)^2 + \int_{\Omega} \left( \frac{\varepsilon^2}{2} |\nabla \phi|^2 + F(\phi) \right) d\mathbf{x}. \quad (5)$$

Here,  $\eta$  is the Lagrangian multiplier and  $\beta$  is a positive penalty factor. The last term in Eq. (5) represents the Ginzburg-Landau free energy [49], in which  $\varepsilon$  is the thickness of the diffusive interface and  $F(\phi) = 0.25\phi^2(1-\phi)^2$  is the double well potential. According to the principle of  $L^2$ -gradient flow [50,51] of the energy Eq. (5), the original phase field evolution equation for  $\phi$  with time  $t$  is obtained:

$$\begin{aligned} \phi_t &= -\frac{\partial E(\phi, \mathbf{u})}{\partial \phi} = -\eta q \phi^{q-1} W_0(\mathbf{u}) - \beta (V(\phi) - V_0) + \varepsilon^2 (\nabla^2 \phi - \frac{F'(\phi)}{\varepsilon^2}), \\ W_0(\mathbf{u}) &= \frac{1}{2} \varepsilon(\mathbf{u}) : \mathbf{D}^0 : \varepsilon(\mathbf{u}). \end{aligned} \quad (6)$$

Here the Neumann boundary condition  $\mathbf{n} \cdot \nabla \phi = 0$  is used.

## 2.2. Precondition modification equation

For traditional phase field based topology optimization method, the phase field equation Eq. (6) has the motion of the mean curvature [52]. To ensure that our purpose of minimizing the objective function is not interfered by the curvature effects, we are committed to remove the impact of curvature effects included in Eq. (6). Inspired by the anti-diffusive phase-field equation proposed by Chiu and Lin [28], we use the signed distance function to define  $\phi$ , i.e.  $\phi = (1 + \tanh(s/2\varepsilon))/2$ . The first and second order derivatives of  $\phi$  can be expressed explicitly as follows:

$$|\nabla \phi| = \frac{\partial \phi}{\partial s} = \frac{\phi(1-\phi)}{\varepsilon}, \quad (7)$$

$$\frac{(\nabla \phi \cdot \nabla) |\nabla \phi|}{|\nabla \phi|} = |\nabla^2 \phi| = \frac{\partial^2 \phi}{\partial s^2} = \frac{\phi(1-\phi)(1-2\phi)}{\varepsilon^2}. \quad (8)$$

Here  $\varepsilon$  controls the thickness of the interface. And  $\hat{\mathbf{n}} = \nabla \phi / |\nabla \phi|$  is the unit normal vector on interface. In addition, we can get

$$\kappa = \nabla \cdot \hat{\mathbf{n}} = \nabla \cdot \frac{\nabla \phi}{|\nabla \phi|} = \frac{1}{|\nabla \phi|} \left( \nabla^2 \phi - \frac{(\nabla \phi \cdot \nabla) |\nabla \phi|}{|\nabla \phi|} \right). \quad (9)$$

Note that  $\kappa$  represents the curvature of the interface, which is widely available in traditional phase field models, such as the reaction-

diffusion term in Eq. (6). However, the aim of problem Eq. (1) is to minimize only the actual objective function  $J(\phi)$  with the volume constraint, thus the impact of curvature should be eliminated from the original evolution equation. Combining Eq. (6) with Eq. (9), we substitute the reaction-diffusion term into a penalty term to eliminate the curvature effects. Therefore our evolution equation is given

$$\begin{aligned} \phi_t &= -\eta q \phi^{q-1} W_0(\mathbf{u}) - \beta (V(\phi) - V_0) \\ &\quad + \gamma \left( \nabla^2 \phi - \frac{\phi(1-\phi)(1-2\phi)}{\varepsilon^2} - |\nabla \phi| \nabla \cdot \hat{\mathbf{n}} \right). \end{aligned} \quad (10)$$

Here  $\gamma$  is the penalty coefficient. Note that in Eq. (10), the curvature-driven interface motion is eliminated, because the last term in the right side of Eq. (10) can be reorganized as follows:

$$\begin{aligned} &\gamma \left( \nabla^2 \phi - \frac{\phi(1-\phi)(1-2\phi)}{\varepsilon^2} - |\nabla \phi| \nabla \cdot \hat{\mathbf{n}} \right) \\ &= \gamma \left( \nabla^2 \phi - \frac{(\nabla \phi \cdot \nabla) |\nabla \phi|}{|\nabla \phi|} - |\nabla \phi| \nabla \cdot \hat{\mathbf{n}} \right) = \gamma (|\nabla \phi| \nabla \cdot \hat{\mathbf{n}} - |\nabla \phi| \nabla \cdot \hat{\mathbf{n}}) = 0. \end{aligned} \quad (11)$$

Using Eq. (8), we can collect the last term in the right side of Eq. (10), now the modified evolution equation is derived

$$\phi_t = -\eta q \phi^{q-1} W_0(\mathbf{u}) - \beta (V(\phi) - V_0) + \bar{\gamma} (\varepsilon \nabla \cdot \nabla \phi - \nabla \cdot (\phi(1-\phi)\hat{\mathbf{n}})), \quad (12)$$

where  $\bar{\gamma} = \gamma/\varepsilon$ . In this paper, we choose  $\gamma = \varepsilon^2$  for formulation. The Neumann boundary condition  $\hat{\mathbf{n}} \cdot \nabla \phi = 0$  is concerned.

After we eliminate the curvature effects from the original phase field function, the energy function corresponding to the modified phase field equation Eq. (12) can be rewritten as

$$\tilde{E}(\phi, \mathbf{u}) = \eta \int_{\Omega} W(\phi, \mathbf{u}) d\mathbf{x} + \frac{\beta}{2} (V(\phi) - V_0)^2, \quad (13)$$

which contains only the virtual work and the penalty term of volume constraint. Now we can prove that the energy  $\tilde{E}(\phi, \mathbf{u})$  holds the law of energy dissipation:

$$\begin{aligned} \frac{d}{dt} \tilde{E}(\phi, \mathbf{u}) &= \frac{\partial \tilde{E}}{\partial \phi} \phi_t + \frac{\partial \tilde{E}}{\partial \mathbf{u}} \mathbf{u}_t \\ &= \int_{\Omega} \left( \eta \frac{\partial W}{\partial \phi} + \beta (V(\phi) - V_0) \right) \phi_t d\mathbf{x} + \varepsilon^2 \int_{\partial\Omega} \hat{\mathbf{n}} \cdot \nabla \phi \phi_t d\tau \\ &= \int_{\Omega} \left( -\phi_t + \bar{\gamma} (\varepsilon \nabla \cdot \nabla \phi - \nabla \cdot (\phi(1-\phi)\hat{\mathbf{n}})) \right) \phi_t d\mathbf{x} \\ &= - \int_{\Omega} \phi_t^2 d\mathbf{x} \leq 0. \end{aligned}$$

We should emphasize that the second equation holds due to  $\frac{\partial \tilde{E}}{\partial \mathbf{u}} \mathbf{u}_t = 0$  in static elasticity, meanwhile the fourth equation holds due to Eq. (11).

The modified equation Eq. (12) enables us to capture the sharp interfaces of  $\phi$ . However, the issue of ill-conditioned behavior of the normal vector occurs during evolution (see in Section 4.1). The reason for this phenomenon is, the above discussion is based on the premise that  $\phi$  must satisfy the signed distance function  $\phi = (1 + \tanh(s/2\varepsilon))/2$ . However, as the iteration proceeds, such a condition is not guaranteed to be satisfied. This leads to an inaccurate calculation of the derivatives and normal vector. The ill condition of normal vector, especially away from the interface, will bring erroneous estimate of interface location and thickness. The problem is also observed in level-set model [53,54]. In order to maintain the interfaces accurately, non-linear precondition process is required [43,55]. Jabir [44] derives the precondition equation based on level-set model in computational fluid dynamics. In this paper, an additional phase-field equation using the signed distance function for normal vector correction is established:

$$\frac{\partial \psi}{\partial \tau} = \varepsilon_0 \Delta \psi + (|\nabla \psi| - 1) \tanh \left( \hat{\beta} \frac{\psi_0}{|\nabla \psi_0|} \right). \quad (14)$$

Here  $\psi_0 = \epsilon \ln(\phi/(1-\phi))$  is the initial value of equation (14),  $\hat{\beta}$  is the interface sharpness parameter,  $\epsilon_0$  is a infinitesimal positive value.  $\psi$  is independently evolved until it converges to sign distance field under the pseudo-time  $\tau$  which is irrelevant to the physical problem. In our study, proceeding preconditioning procedure every 800 physical time steps is used to obtain satisfactory results.

### 3. Numerical implementation

#### 3.1. Numerical method

In this section, a hybrid numerical method based on operator splitting scheme is proposed for solving the modified phase-field evolution equation Eq. (12). Assume the design domain is  $\Omega = (0, L_x) \times (0, L_y)$ ,  $N_x$  and  $N_y$  are positive even integers which satisfy  $L_x/N_x = L_y/N_y$ , then the design domain is discretized with the uniform grid size  $h = L_x/N_x$ . The discrete computational domain is defined as  $\Omega_h = \{(x_i, y_j) | x_i = (i-0.5)h, y_j = (j-0.5)h, 1 \leq i \leq N_x, 1 \leq j \leq N_y\}$ , which consists the set of cell centers. Time step is set to  $\Delta t$ , the approximation of  $\phi(x_i, y_j)$  at time  $n\Delta t$  is recorded as  $\phi_{i,j}^n$ . The splitting scheme for Eq. (3) and (12) is:

$$\nabla \cdot \sigma(\phi^n, \mathbf{u}^{n+1}) = \nabla \cdot (g(\phi^n) \mathbf{D}^0 : \epsilon(\mathbf{u}^{n+1})) = 0, \quad (15)$$

$$\frac{\phi^* - \phi^n}{\Delta t} = -(\lambda \phi^n + \lambda \phi^*) - \eta q W_0(\mathbf{u}^{n+1})(\phi^n)^{q-1} - \beta(V_d(\phi^*) - V_0), \quad (16)$$

$$\frac{\phi^{n+1} - \phi^*}{\Delta t} = \tilde{\gamma}(\epsilon \nabla \cdot \nabla \phi^* - \nabla \cdot (\phi^*(1-\phi^*)\hat{\mathbf{n}})). \quad (17)$$

Where  $\lambda$  is a stabilizing parameter,  $V_d(\phi) = h^2 \sum_i^{N_x} \sum_j^{N_y} \phi_{i,j}$  in Eq. (16) and  $\hat{\mathbf{n}} = \nabla \phi^* / |\nabla \phi^*|$  in Eq. (17). Note that the boundary conditions for  $\mathbf{u}^{n+1}$  in Eq. (15) are:

$$\begin{cases} \mathbf{u}^{n+1} = 0, & \text{on } \Gamma_1 \subset \partial\Omega, \\ \mathbf{n} \cdot \sigma(\phi^n, \mathbf{u}^{n+1}) = \mathbf{s}, & \text{on } \Gamma_2 \subset \partial\Omega, \\ \mathbf{n} \cdot \sigma(\phi^n, \mathbf{u}^{n+1}) = 0, & \text{on } \partial\Omega / (\Gamma_1 \cup \Gamma_2). \end{cases} \quad (18)$$

And the discrete Neumann boundary conditions is used for phase field function.

Next we give the discrete solutions for Eq. (15)-(17) respectively. For the equilibrium equation in Eq. (15) with boundary conditions Eq. (18), we can obtain the updated displacements  $\mathbf{u}^{n+1}$  by finite element method. The term  $V_d(\phi^*)$  in Eq. (16) is difficult to compute directly due to the presence of the implicit form, thus we sum over the index  $i, j$  for  $\phi$  at both sides of Eq. (16) and then multiply  $h^2$ . Therefore  $V_d(\phi^*)$  can be expressed:

$$V_d(\phi^*) = \frac{(\frac{1}{\Delta t} + \lambda)V_d(\phi^n) - \sum_i^{N_x} \sum_j^{N_y} \eta q h^2 (\phi^n)^{q-1} W_0(\mathbf{u}_{i,j}^{n+1}) + \beta N_x N_y V_0 h^2}{\frac{1}{\Delta t} + \lambda + \beta N_x N_y h^2}. \quad (19)$$

Then we obtain the intermediate phase field function  $\phi^*$ :

$$\phi^* = \phi^n - \frac{\eta q W_0(\mathbf{u}^{n+1})(\phi^n)^{q-1} + \beta(V_d(\phi^*) - V_0)}{\lambda + \frac{1}{\Delta t}}, \quad (20)$$

the terms  $W_0(\mathbf{u}^{n+1})$  and  $\epsilon(\mathbf{u}^{n+1})$  are computed as:

$$W_0(\mathbf{u}^{n+1}) = \frac{1}{2} \epsilon(\mathbf{u}^{n+1}) : \mathbf{D}^0 : \epsilon(\mathbf{u}^{n+1}),$$

$$\epsilon(\mathbf{u}^{n+1}) = \frac{1}{2} (\nabla_d \mathbf{u}^{n+1} + (\nabla_d \mathbf{u}^{n+1})^T).$$

Here, the discrete gradient operator  $\nabla_d$  is defined as follows:

$$\nabla_d u_{i,j} = (D_x u_{i+\frac{1}{2},j}, D_y u_{i,j+\frac{1}{2}}), \quad D_x u_{i+\frac{1}{2},j} = \frac{u_{i+1,j} - u_{i,j}}{h},$$

$$D_y u_{i,j+\frac{1}{2}} = \frac{u_{i,j+1} - u_{i,j}}{h}.$$

Furthermore, Eq. (17) is an explicit scheme for the modified term of Eq. (12), and its spatially discretization scheme is given. Let  $\mathbf{m}$  be the

gradient vector at the cell corner, and  $\tilde{\nabla}_d^c \phi_{i,j}^*$  is the gradient vector at the position  $(x_i, y_j)$ . Nine point terms from vertex centered normals [56] are used to discretize the last term of Eq. (12), i.e.  $\nabla \cdot (\phi^*(1-\phi^*)\hat{\mathbf{n}})$ . We first give the following discretization scheme:

$$\tilde{\nabla}_d^c \cdot \left( \frac{\mathbf{m}}{|\mathbf{m}|} \right)_{i,j} = \frac{1}{2h} \left( \frac{m_x^{i+\frac{1}{2},j+\frac{1}{2}}}{|\mathbf{m}_{i+\frac{1}{2},j+\frac{1}{2}}|} + \frac{m_x^{i+\frac{1}{2},j-\frac{1}{2}}}{|\mathbf{m}_{i+\frac{1}{2},j-\frac{1}{2}}|} - \frac{m_x^{i-\frac{1}{2},j+\frac{1}{2}}}{|\mathbf{m}_{i-\frac{1}{2},j+\frac{1}{2}}|} - \frac{m_x^{i-\frac{1}{2},j-\frac{1}{2}}}{|\mathbf{m}_{i-\frac{1}{2},j-\frac{1}{2}}|} \right. \\ \left. + \frac{m_y^{i+\frac{1}{2},j+\frac{1}{2}}}{|\mathbf{m}_{i+\frac{1}{2},j+\frac{1}{2}}|} + \frac{m_y^{i-\frac{1}{2},j+\frac{1}{2}}}{|\mathbf{m}_{i-\frac{1}{2},j+\frac{1}{2}}|} - \frac{m_y^{i+\frac{1}{2},j-\frac{1}{2}}}{|\mathbf{m}_{i+\frac{1}{2},j-\frac{1}{2}}|} - \frac{m_y^{i-\frac{1}{2},j-\frac{1}{2}}}{|\mathbf{m}_{i-\frac{1}{2},j-\frac{1}{2}}|} \right).$$

Here  $\mathbf{m}_{i+\frac{1}{2},j+\frac{1}{2}} = (m_x^{i+\frac{1}{2},j+\frac{1}{2}}, m_y^{i+\frac{1}{2},j+\frac{1}{2}})$ , and  $m_x^{i+\frac{1}{2},j+\frac{1}{2}}$  and  $m_y^{i+\frac{1}{2},j+\frac{1}{2}}$  are formulated as follows:

$$m_x^{i+\frac{1}{2},j+\frac{1}{2}} = \frac{\phi_{i+1,j+1}^* + \phi_{i+1,j}^* - \phi_{i,j+1}^* - \phi_{i,j}^*}{2h}, \quad m_y^{i+\frac{1}{2},j+\frac{1}{2}} = \frac{\phi_{i+1,j+1}^* + \phi_{i,j+1}^* - \phi_{i+1,j}^* - \phi_{i,j}^*}{2h},$$

which represent the components of normal vector located at the top right vertex of cell  $(i, j)$ . By averaging the four vertex gradient vectors of cell  $(i, j)$ , we can obtain the discrete gradient  $\tilde{\nabla}_d^c \phi_{i,j}^*$  and the unit normal vector  $\hat{\mathbf{n}}_{i,j}$  at cell center  $(x_i, y_j)$ :

$$\tilde{\nabla}_d^c \phi_{i,j}^* = \frac{1}{4} (\mathbf{m}_{i+\frac{1}{2},j+\frac{1}{2}} + \mathbf{m}_{i+\frac{1}{2},j-\frac{1}{2}} + \mathbf{m}_{i-\frac{1}{2},j+\frac{1}{2}} + \mathbf{m}_{i-\frac{1}{2},j-\frac{1}{2}}), \quad (21)$$

$$\hat{\mathbf{n}}_{i,j} = \frac{\tilde{\nabla}_d^c \phi_{i,j}^*}{|\tilde{\nabla}_d^c \phi_{i,j}^*|}.$$

Now we can calculate  $\tilde{\nabla}_d^c \cdot (\phi^*(1-\phi^*)\hat{\mathbf{n}})$  at  $(x_i, y_j)$  in a similar way:

$$\tilde{\nabla}_d^c \cdot (\phi^*(1-\phi^*)\hat{\mathbf{n}})_{i,j} = \frac{1}{2h} \left( \phi_{i+\frac{1}{2},j+\frac{1}{2}}^* (1-\phi_{i+\frac{1}{2},j+\frac{1}{2}}^*) \frac{m_x^{i+\frac{1}{2},j+\frac{1}{2}}}{|\mathbf{m}_{i+\frac{1}{2},j+\frac{1}{2}}|} \right. \\ + \phi_{i+\frac{1}{2},j-\frac{1}{2}}^* (1-\phi_{i+\frac{1}{2},j-\frac{1}{2}}^*) \frac{m_x^{i+\frac{1}{2},j-\frac{1}{2}}}{|\mathbf{m}_{i+\frac{1}{2},j-\frac{1}{2}}|} \\ - \phi_{i-\frac{1}{2},j+\frac{1}{2}}^* (1-\phi_{i-\frac{1}{2},j+\frac{1}{2}}^*) \frac{m_x^{i-\frac{1}{2},j+\frac{1}{2}}}{|\mathbf{m}_{i-\frac{1}{2},j+\frac{1}{2}}|} \\ - \phi_{i-\frac{1}{2},j-\frac{1}{2}}^* (1-\phi_{i-\frac{1}{2},j-\frac{1}{2}}^*) \frac{m_x^{i-\frac{1}{2},j-\frac{1}{2}}}{|\mathbf{m}_{i-\frac{1}{2},j-\frac{1}{2}}|} \\ + \phi_{i+\frac{1}{2},j+\frac{1}{2}}^* (1-\phi_{i+\frac{1}{2},j+\frac{1}{2}}^*) \frac{m_y^{i+\frac{1}{2},j+\frac{1}{2}}}{|\mathbf{m}_{i+\frac{1}{2},j+\frac{1}{2}}|} \\ + \phi_{i-\frac{1}{2},j+\frac{1}{2}}^* (1-\phi_{i-\frac{1}{2},j+\frac{1}{2}}^*) \frac{m_y^{i-\frac{1}{2},j+\frac{1}{2}}}{|\mathbf{m}_{i-\frac{1}{2},j+\frac{1}{2}}|} \\ - \phi_{i+\frac{1}{2},j-\frac{1}{2}}^* (1-\phi_{i+\frac{1}{2},j-\frac{1}{2}}^*) \frac{m_y^{i+\frac{1}{2},j-\frac{1}{2}}}{|\mathbf{m}_{i+\frac{1}{2},j-\frac{1}{2}}|} \\ \left. - \phi_{i-\frac{1}{2},j-\frac{1}{2}}^* (1-\phi_{i-\frac{1}{2},j-\frac{1}{2}}^*) \frac{m_y^{i-\frac{1}{2},j-\frac{1}{2}}}{|\mathbf{m}_{i-\frac{1}{2},j-\frac{1}{2}}|} \right),$$

where  $\phi_{i+\frac{1}{2},j+\frac{1}{2}}^* = \frac{1}{4}(\phi_{i+1,j+1}^* + \phi_{i+1,j}^* + \phi_{i,j+1}^* + \phi_{i,j}^*)$ .

Meanwhile, the discrete nine point Laplacian operator  $\Delta_d^e$  at  $(x_i, y_j)$  [56] is defined as:

$$\Delta_d^e \phi_{i,j}^* = \frac{1}{6h^2} (\phi_{i+1,j+1}^* + \phi_{i+1,j-1}^* + \phi_{i-1,j+1}^* + \phi_{i-1,j-1}^* \\ + 4\phi_{i,j-1}^* + 4\phi_{i,j+1}^* + 4\phi_{i+1,j}^* + 4\phi_{i-1,j}^* - 20\phi_{i,j}^*). \quad (22)$$

Thus the updated phase field function  $\phi^{n+1}$  is obtained:



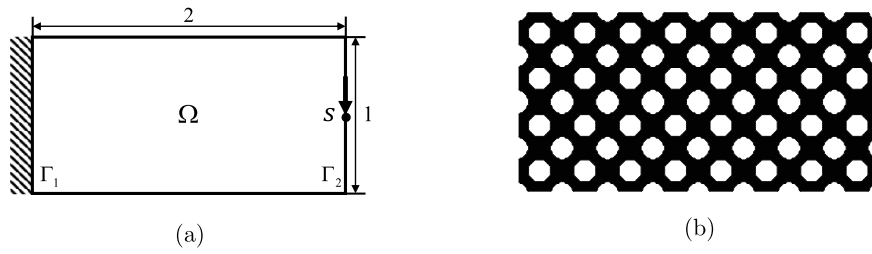


Fig. 1. The design domain (a) and initial shape (b) for the stiffness maximization simulations of a cantilever.

$$\phi^{n+1} = \phi^* + \Delta t \tilde{\gamma} \left( \epsilon \Delta_d^e \phi^* - \tilde{\nabla}_d^c \cdot (\phi^* (1 - \phi^*) \hat{\mathbf{n}}) \right). \quad (23)$$

The similar discretization scheme of the precondition equation can also be obtained (14):

$$\frac{\psi^{k+1} - \psi^k}{\Delta \tau} = \epsilon_0 \Delta_d^e \psi^k + (|\tilde{\nabla}_d^c \psi^k| - 1) \tanh \left( \frac{\hat{\beta} \psi_0}{|\tilde{\nabla}_d^c \psi_0| + \text{tol}} \right), \quad (24)$$

where  $\Delta_d^e \psi^k$  and  $\tilde{\nabla}_d^c \psi^k$  are similarly defined as Eq. (22) and Eq. (21), respectively. It is worth noting that  $\text{tol}$  is a positive parameter in order to avoid singular values during the calculation, which is set to a small value  $10^{-5}$ .

### 3.2. Optimization algorithm

Based on the above discussion, we introduce an iterative procedure to update the phase field variable  $\phi$ , in which the displacement  $\mathbf{u}$  decouples with  $\phi$ , the precondition process will be carried out when the iteration reaches a certain number of steps. The optimization algorithm procedure is constructed as follows:

- Step 1.** Instantiate the phase-field and finite element meshes for entire design domain  $\Omega$ , set the initial phase field function  $\phi^0$ .
- Step 2.** Solve equilibrium equation Eq. (3) and Eq. (4) with respect to  $\phi^n$  at  $n$ -th iteration to obtain the displacement field  $\mathbf{u}^{n+1}$  by finite element method.
- Step 3.** Solve the modified phase-field equation Eq. (12) to update  $\phi^{n+1}$ .
- Step 4.** Carry out precondition process every 800 time steps:
  - (a) Introduce signed distance function  $\psi$  and set  $\psi^0 = \epsilon \ln(\phi/(1 - \phi))$ .
  - (b) Use precondition process equation Eq. (14) to update  $\psi$  under the pseudo-time  $\tau$  until convergence.
  - (c) Define  $\phi = (1 + \tanh(\psi/2\epsilon))/2$ , and go back to step 2.
- Step 5.** Check convergence. If  $\|\phi^{n+1} - \phi^n\|_{L^2} < 10^{-6}$ , proceed to step 6, otherwise go back to step 2.
- Step 6.** Obtain the optimal distribution of  $\phi$  and the optimal shape of design domain.

## 4. Numerical results

This section provides several numerical tests to demonstrate the practicability of the proposed method. Unless stated otherwise, the parameters of the material in all experiments are set as Poisson's ratio  $\nu = 0.3$ , elasticity modulus  $E = 1$  and  $g_{\min} = 10^{-4}$ . The interface sharpness parameter  $\hat{\beta}$  in preconditioning equation Eq. (14) is set to  $3p/4h$  with  $p = 4$  [44], the stabilizing parameter in Eq. (16) is set to  $\lambda = 0.5$ .

### 4.1. Topology optimization of cantilever beam

Firstly, classical stiffness maximization simulations of a cantilever beam with a traction force  $s$  on the boundary is considered. The design domain  $\Omega = (0, 2) \times (0, 1)$  and the initial shape are shown in Fig. 1(a) and Fig. 1(b), respectively. The left side of the design domain is fixed while a traction force  $s$  is loaded at the middle of the right side. A  $200 \times 100$  rectangular mesh is used to discretize the domain. We set

$\epsilon = 0.03$  to control the width of the interface, while  $\beta = 10$  and  $\eta$  is chosen from  $[1, 10]$  according to [7]. Time step is set to  $\Delta t = 0.9h^2/(2\epsilon^2)$ . Therefore the CFL condition is satisfied. Fig. 2(a)–(c) show the topology evolutions using the original phase field model proposed by [25], our model without the precondition process Eq. (12) and our model with the precondition process Eq. (12) and Eq. (14) at certain specific moments, respectively. The convergence histories of energy for different models are shown in Fig. 3.

As shown in Figs. 2 and 3, the energy corresponding to the original phase field model (a) is quite different from the energy corresponding to the present model (b) and (c). This phenomenon supports that by the original phase field model, the migration of interface is driven not only by the strain energy and volume constraint, but also the curvature effect, which leads to the final topology coarsen gradually and continuously. Therefore the structure details lost. However, our scheme Eq. (12) and Eq. (14) can significantly reduce the curvature effect, which efficiently increases the stiffness. Our method works well and can remain a clear result. In addition, we note that our model plays a similar role in eliminating the curvature effect as Takaki's analysis, the topological evolution process is almost same as the results in [39], while our model contains more details on each beam.

Comparing the results shown in Fig. 2(b) and Fig. 2(c), the role of the precondition equation Eq. (14) in the evolution process can be intuitively and clearly demonstrated. In the early stage of evolution, the results of the two models are almost the same. However, for the model without the preconditioning process, the symmetry of topology is destroyed as the time evolving, and finally leads to the asymmetric deformation structures shown in the last picture of Fig. 2(b). This is mainly due to the ill conditioned error estimation of normal vector if only Eq. (12) is used, which will cause a large error in the estimation of interface position and thickness. The problem can be well alleviated by precondition equation Eq. (14), which is an alternative preconditioning method for normal vector correction. To further show this, we calculate the difference between  $\epsilon|\nabla\phi|$  and  $\phi(1 - \phi)$  to verify whether the values of  $\phi$  corresponding to Figs. 2(b) and 2(c) satisfy the condition of signed distance function. The results are shown in Fig. 4. Obviously the  $\phi$  corresponding to Fig. 2(b) does not satisfy the premise of the signed distance function, but the preconditioning process can solve this problem. Hence, our model with preconditioning process can make the results sufficiently accurate and remain more topology details, as shown in Fig. 2(c).

### 4.2. Topology optimization of short cantilever beam

Next, we consider the impact of initial conditions through the short cantilever beam [47], which is a well-known structure in the field of topology optimization. The design domain  $\Omega = (0, 1) \times (0, 1)$  is shown in Fig. 5. The left side of the design domain is fixed, while a single vertical load  $s = 1$  is applied at the right bottom corner of the design domain. The fixed design domain is discretized using  $100 \times 100$  elements for finite element analysis. Three cases with different initial shapes are studied in which the number of holes distributed is set to  $3 \times 3$ ,  $4 \times 4$  and  $5 \times 5$ , respectively. Fig. 6 shows three cases and their obtained optimized configurations. The convergence histories of structural compliance  $J(\phi)$  and normalized compliance  $J(\phi)/J(\phi_0)$  for different initial

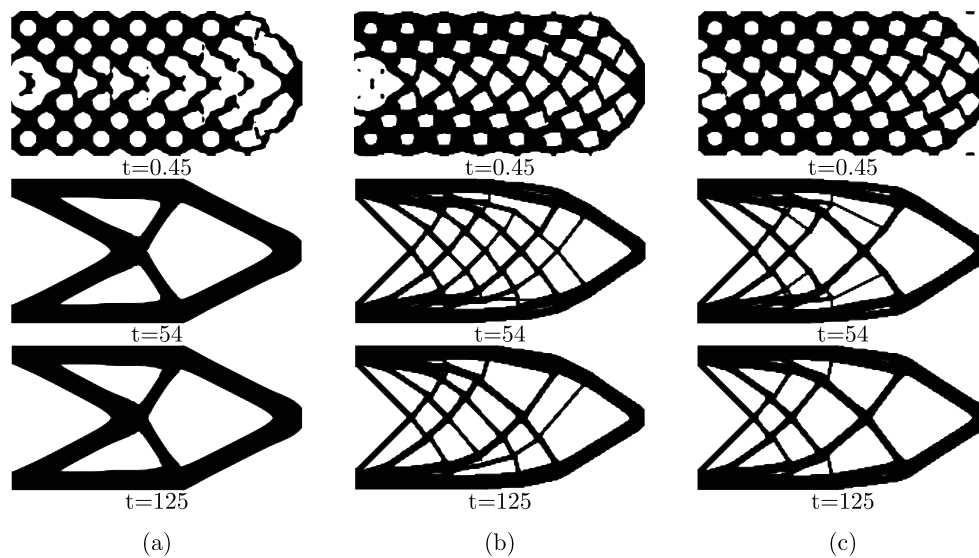


Fig. 2. Evolutions using (a) the original phase field model, (b) our model without the precondition process and (c) our model with the precondition process.

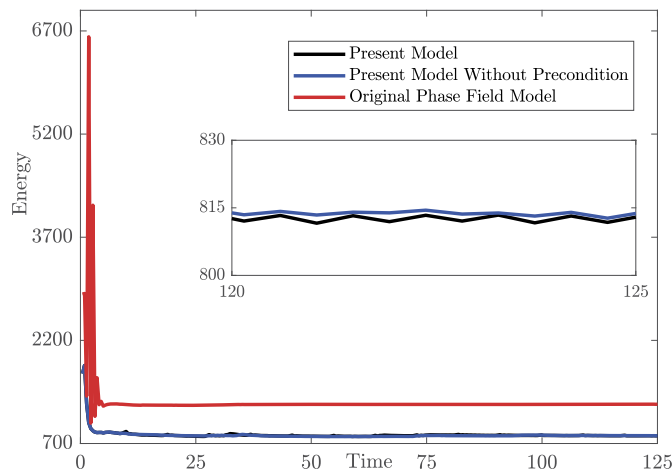


Fig. 3. The convergence histories of energy for different models.

shapes are provided in Fig. 7. The results confirm the effect of initial configurations. For different studied cases, more complex initial topology, reflecting as more holes in the initial design domain, will lead to the complexity of the final topology. These findings are understandable, because the original phase field equation maintains the coarse support, while our present method can provide detailed branches for the coarse support, making the whole structure more rigid. This effect becomes more pronounced with the increase of the initial holes.

To verify the extensive applicability of the present model, we focus on the topology optimization with the random initial condition. The initial condition is set randomly from 0 to 1 throughout the design domain, as shown in the first image of Fig. 8. The evolutions with the random initial shapes are shown in Fig. 8. The results confirm that the present model works well for arbitrary initial conditions.

#### 4.3. Topology optimization of bridge

In this section, we apply our model to the bridge structure example, which is also called the Michell type structure with fixed-fixed supports. The design domain  $\Omega = (0, 2) \times (0, 1)$  and the initial shape are shown in Fig. 9(a) and Fig. 9(b), respectively. In this problem, the corners on both left and right sides are fixed, and there is a unit point force loaded on the center of the bottom. The design domain is discretized using  $200 \times 100$  rectangular mesh. Other parameters are set as  $\epsilon = 0.03$ ,  $\eta = 1.0$ ,  $\beta = 10$ ,

$\Delta t = 0.9h^2/(2\epsilon^2)$ . Meanwhile, in order to verify effects of the volume constraints, we set different values of  $V_0$  with 0.2, 0.4 and 0.6. The final optimization results and the convergence histories of the total volume are shown in Fig. 10 and Fig. 11 respectively. We can see from Fig. 10 that the volume constraint will not only affect the width of the beam, but also the number and size of nucleation of holes. Furthermore Fig. 11 investigates that our model can well maintain volume constraints.

Fig. 12 shows the evolution process of the normalized energy  $\tilde{E}(\phi_n)/\tilde{E}(\phi_0)$  for  $V_0 = 0.4$ , where the energy decreases fast at early several steps and the structure topologies change violently. The final topology keeps a stable state when the evolution reaches convergence. Note that although we have proved the energy dissipation of Eq. (12) in Section 2.2, our model is not globally energy decreasing. Some unsmooth cusp points appear in Fig. 12 during the evolution process. These cusp points are mainly caused by the implementation of precondition, and each completed precondition process is accompanied by the appearance of a cusp point. The cusp points are present for every numerical experiment, although they are not so obvious in some situations. However, from Fig. 12 we confirm that our model holds a general trend of decreasing energy even under the influence of the precondition process.

#### 4.4. Topology optimization of Messerschmitt-Bölkow-Blohm beam

In this section, the proposed method is applied to the Messerschmitt-Bölkow-Blohm (MBB) beam. The original problem is shown in Fig. 13(a), where the design domain is  $\Omega = (0, 6) \times (0, 1)$ , the left bottom corner of the beam is pinned while the right bottom corner is supported horizontally [57–60]. Different traction forces  $s$  are applied at the center of the top edge, while other parameters are the same as those in Section 4.3.

Only half of the design domain is considered due to the symmetry, as shown in Fig. 13(b). The rectangular domain  $(0, 3) \times (0, 1)$  is discretized with  $210 \times 70$  square elements. Fig. 14(a) shows the initial shape of half design domain. Fig. 14(b–d) show the final MBB beam topology configurations with different traction forces  $s = (0, 2)$ ,  $(0, 3)$  and  $(0, 4)$ . It is well established that the final material distributions depend on the concentrate forces loaded at the design domain. This demonstrates that the introduction of different forces can greatly affect the final topologies with the same constraint condition. The convergence histories of structural compliance  $J(\phi)$  for different traction forces are shown in Fig. 15, which confirms that the larger traction force results in larger value of compliance.

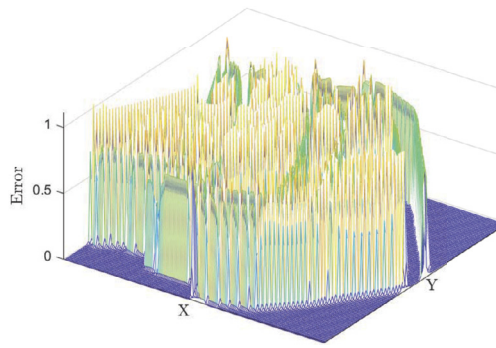


Figure 2 (b)

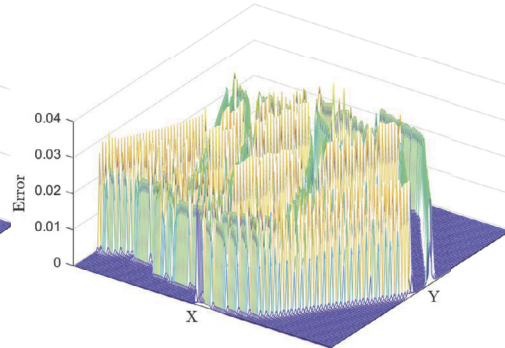


Figure 2 (c)

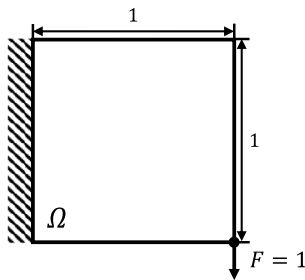
Fig. 4. The mesh plot of  $|\epsilon|\nabla\phi| - \phi(1-\phi)|$  at  $t = 125$ .

Fig. 5. Design domain of the short cantilever problem.

#### 4.5. Planar structure with multiple loads

This section is devoted to the numerical examination of the effect of multiple loads on the final topology through a simply supported planar structure as shown in Fig. 16(a). The design domain is set to  $\Omega = (0, 2) \times (0, 1)$ , and the boundary condition is similar as that in the MBB beam test, where the left bottom corner is clamped with zero displacement and the right bottom corner is only restricted of zero vertical displacement. The entire domain is discretized using a  $200 \times 100$  rectangular mesh. The initial shape of this example is shown in Fig. 16(b).

Fig. 17 shows the final topology under three different force distributions applied to the bottom edge, i.e. (a)  $s_1 = (0, 2), s_2 = s_3 = s_4 = s_5 = 0$ , (b)  $s_1 = (0, 2), s_2 = s_3 = (0, 1), s_4 = s_5 = 0$ , (c)  $s_1 = (0, 2), s_2 = s_3 = (0, 1), s_4 = s_5 = (0, 0.5)$ . The convergence histories of structural compliance for different concentrated force distributions are shown in Fig. 18. We are convinced that with the change of concentrated force distribution, the size, location and quantity of holes in the final topology make difference accordingly, leading more material to meet the concentrated force condition.

#### 4.6. Topology optimization on the complex domain

Topology optimization on the regular rectangular area is not enough for realistic requirements. In this section we make a comment about topology optimization on the complex domain. We focus on elliptical domain, which is shown in Fig. 19(a). The bottom of the design domain is fixed, while two traction forces are loaded at the middle of the left and right side respectively. For the treatment of non-rectangular boundaries, we refer to the calculation method in [61,62]. Fig. 19(b) shows the initial shape and Fig. 20 shows the topology evolutions on the complex domain. We are confident that our model can be successfully extended to irregularly complex regions, thus more practical and complex topology optimization problems can be solved.

#### 4.7. Topology optimization of 3D cantilever beam

The phase field model has the advantage of easy generalization and low computational complexity when considering large scale problems or 3D problems. In this section, our phase field topology optimization model is extended to the three dimensional situation. We consider the topology optimization of 3D cantilever beam on the design domain  $\Omega$ , which is shown in Fig. 21(a). We set  $h = 1/512$  and the mesh size is  $1024 \times 512 \times 16$ . The left side of the design domain is fully constrained, the traction force  $s$  is loaded at the quarter of the right side, while other parameters are the same as those in 2D situation. Fig. 21(b) shows the initial shape and Fig. 22 shows the evolutions of the 3D cantilever beam. The results suggest that the present phase field model can be successfully extended to solve the three-dimensional topology optimization problem and has strong potential for large scale problems.

### 5. Conclusion

In this paper, we proposed a modified phase field method with a nonlinear preconditioning process to deal with topology optimization problems. By introducing a penalty term to replace the reaction diffusion term, the curvature effects could be omitted from the original phase field evolution equation. Meanwhile the ill-conditioned behavior of the normal vector was avoided through preconditioning process, in which the accurate unit normal vector as well as curvature could be obtained. Thus the accurate interface profile could be obtained by the modified phase field method. To implement the numerical algorithm, we used the finite element method, finite difference method and linearly stabilized splitting scheme simultaneously. A series of comparative numerical examples such as cantilever beam, short cantilever beam, bridge, MBB beam, planar structure with multiple loads were presented to demonstrate that the present method could successfully remove the curvature effect without interface deformation problems, thus our method could keep more details in the topology structure. Furthermore, our method could be easily extended to other problems in topology optimization, which implied a wider range of applications in practical topology optimization problems. One limitation of our present implementation is that our method may fail to remove small voids for topological structure, since we have removed the interface motion driven by curvature effects. A proper smooth algorithm needs to be introduced to smooth the connecting boundaries. In the future, we will smooth topological design of structures with minimum and maximum length scales.

#### Data availability

No data was used for the research described in the article.

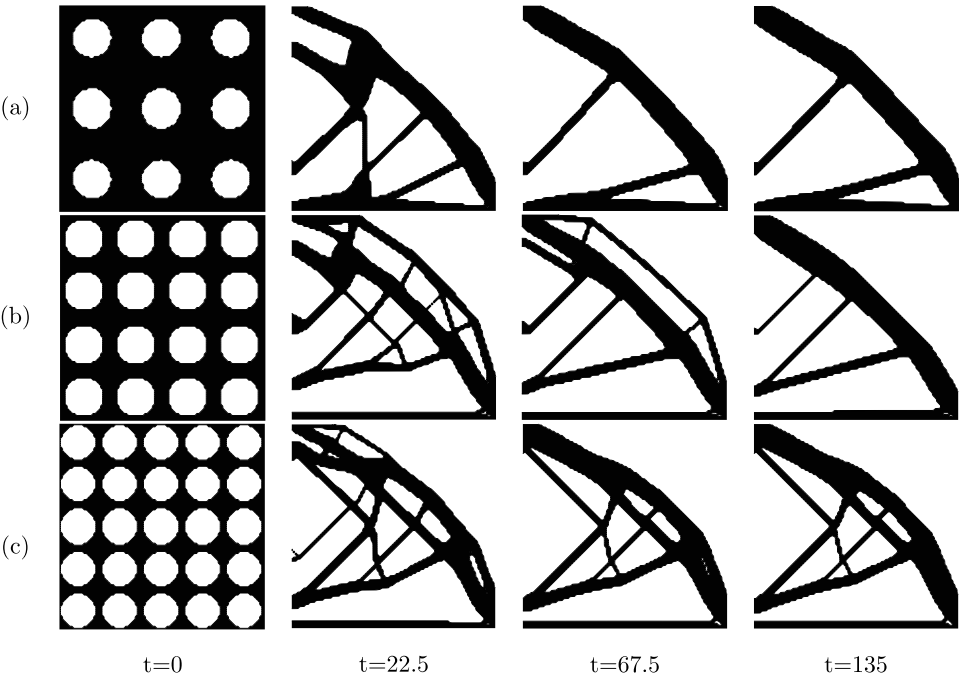


Fig. 6. Evolutions with different initial shapes (a)  $3 \times 3$  holes (b)  $4 \times 4$  holes (c)  $5 \times 5$  holes.

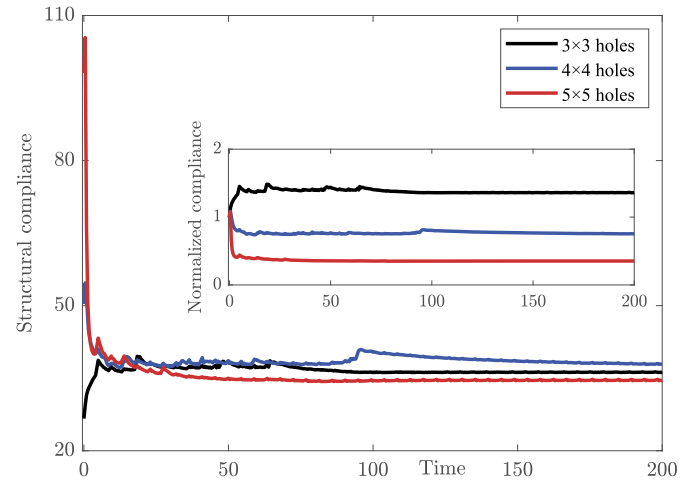


Fig. 7. The convergence histories of structural compliance and normalized compliance for different initial shapes.

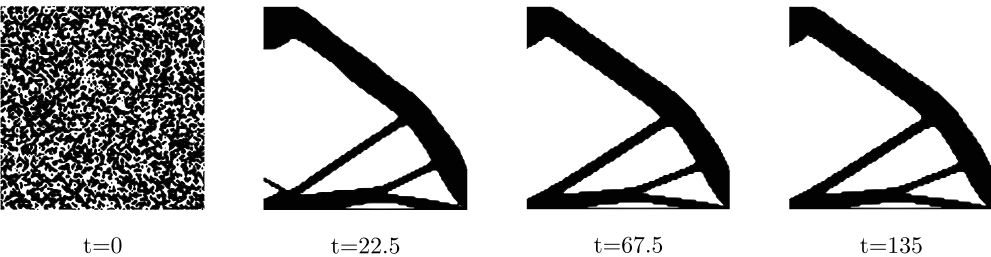
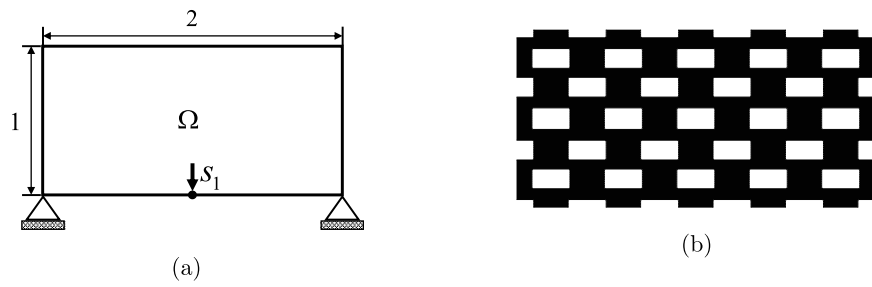
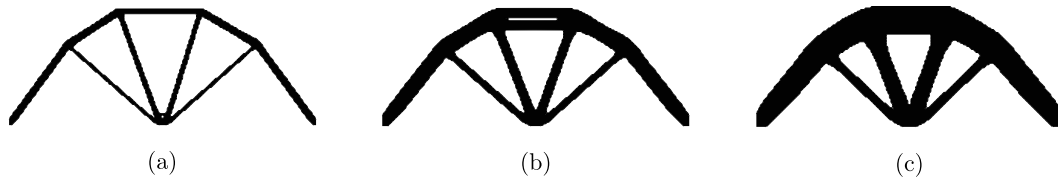


Fig. 8. Evolutions with the random initial shapes.





**Fig. 9.** The optimal configurations for the stiffness maximization simulations of bridge under the same initial shape on mesh  $200 \times 100$ . (a) Schematic illustration. (b) Initial shape.



**Fig. 10.** The final optimization configurations at  $t = 180$  with different values of  $V_0$  under the same initial conditions: (a)  $V_0 = 0.2$ , (b)  $V_0 = 0.4$ , (c)  $V_0 = 0.6$ .

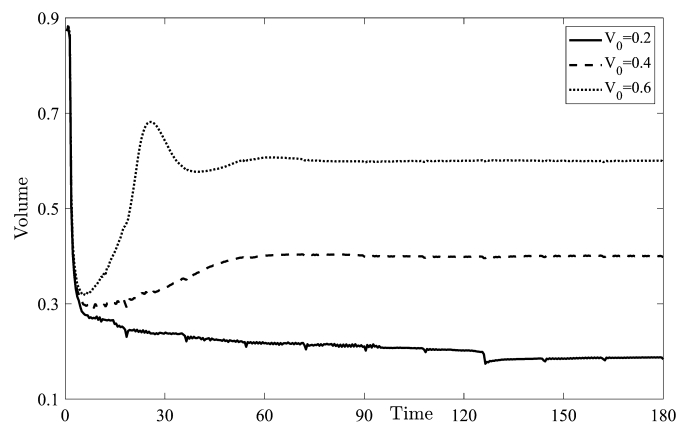


**Fig. 11.** The convergence histories of total volume for  $V_0 = 0.2, 0.4, 0.6$ .

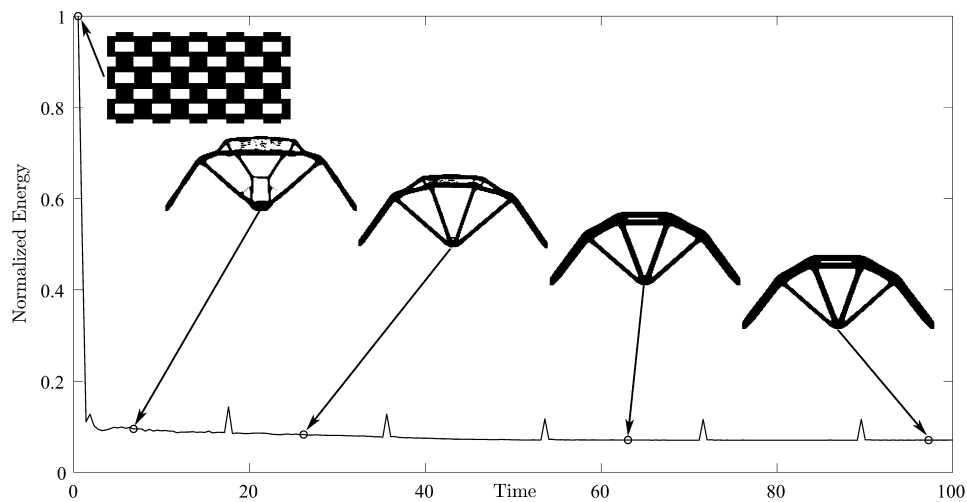


**Fig. 12.** Evolutions of the normalized energy for  $V_0 = 0.4$ .

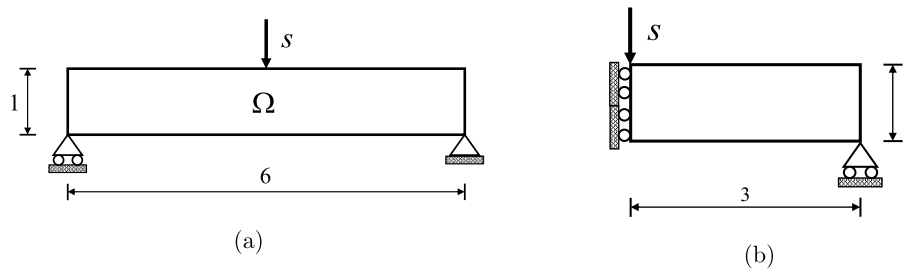


Fig. 13. The full design domain (a) and half design domain with symmetry boundary conditions (b) for MBB beam.

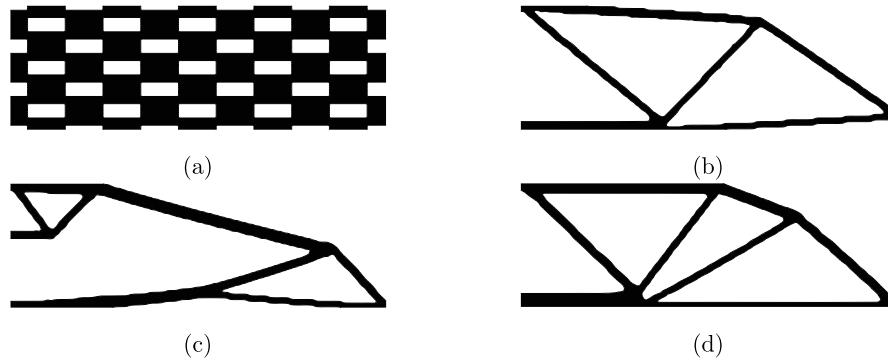


Fig. 14. The initial shape of half design domain (a) and topology configurations for MBB beam with different traction forces, (b)  $s = (0, 2)$ , (c)  $s = (0, 3)$ , (d)  $s = (0, 4)$ .

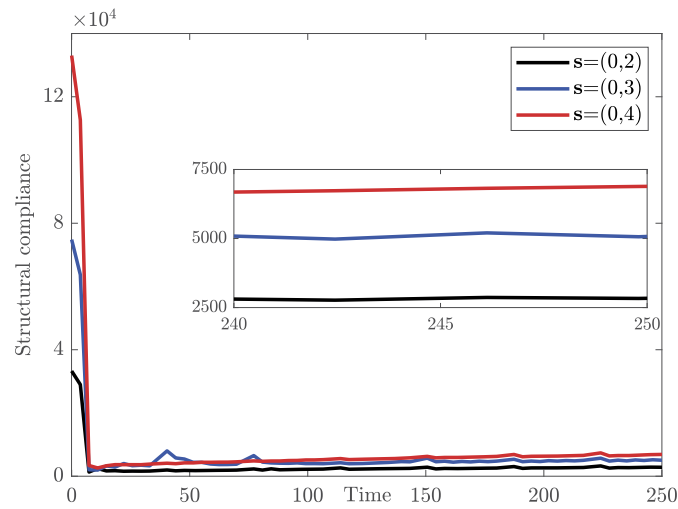


Fig. 15. The convergence histories of structural compliance for different traction forces.

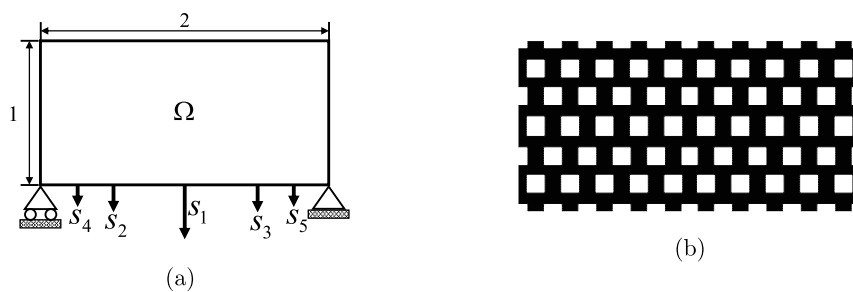
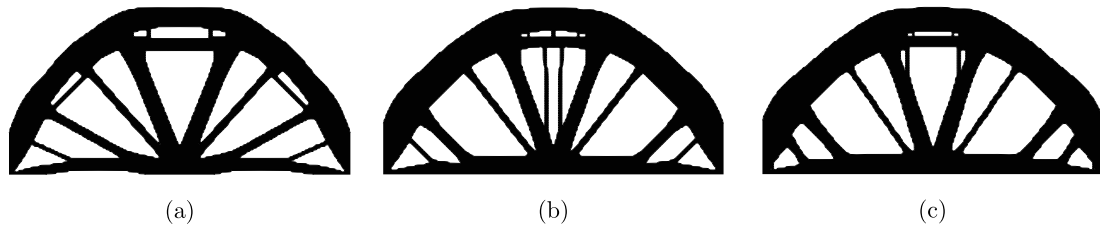
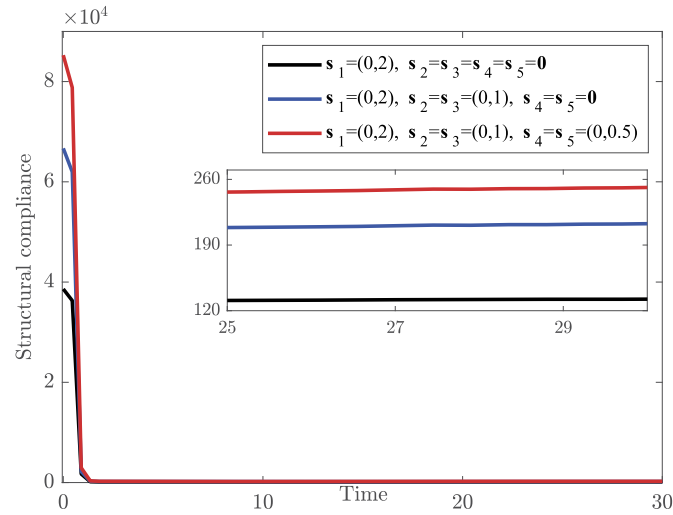


Fig. 16. The design domain (a) and initial shape (b) for planar structure with multiple loads.



**Fig. 17.** The final optimization configurations at  $t = 67.5$  with different concentrated force distributions, (a)  $s_1 = (0, 2), s_2 = s_3 = s_4 = s_5 = 0$ , (b)  $s_1 = (0, 2), s_2 = s_3 = (0, 1), s_4 = s_5 = 0$ , (c)  $s_1 = (0, 2), s_2 = s_3 = (0, 1), s_4 = s_5 = (0, 0.5)$ .



**Fig. 18.** The convergence histories of structural compliance for different concentrated force distributions.

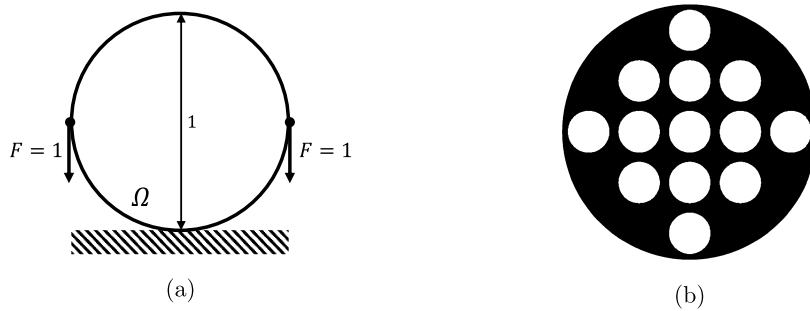


**Fig. 19.** The design domain (a) and initial shape (b) for topology optimization on the complex domain.

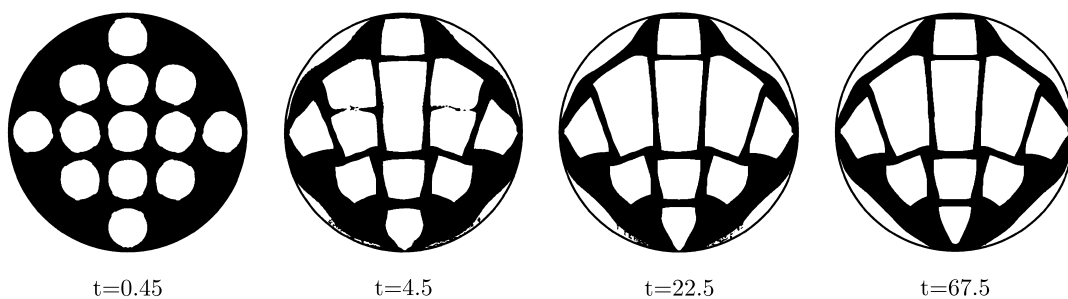


**Fig. 20.** Evolutions of topology optimization on the complex domain.

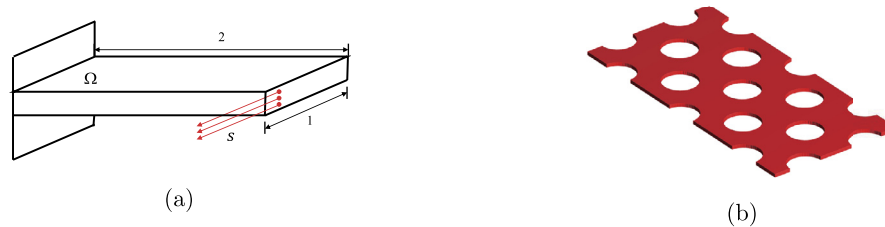


Fig. 21. The design domain (a) and initial shape (b) for topology optimization of 3D cantilever beam.

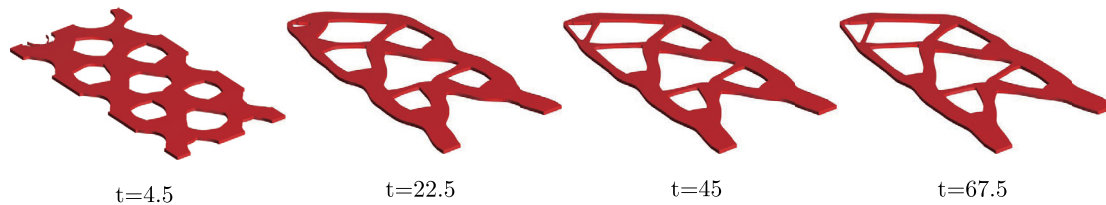


Fig. 22. Evolutions of the 3D cantilever beam.

## Acknowledgement

This work is supported by National Natural Science Foundation of China (No. 12271430). The authors thank the reviewers for the constructive and helpful comments on the revision of this article.

## References

- [1] G. Allaire, Shape Optimization by the Homogenization Method, Springer Verlag, New York, 2001.
- [2] A. Cherkasov, Variational Methods for Structural Optimization, Springer, New York, 2000.
- [3] M.P. Bendsøe, N. Kikuchi, Generating optimal topologies in structural design using a homogenization method, *Comput. Methods Appl. Mech. Eng.* 71 (1988) 197224.
- [4] Q. Yu, Y. Li, Generating optimal topologies in structural design using a homogenization method, *Comput. Methods Appl. Mech. Eng.* 405 (2023) 115876.
- [5] Q. Yu, Q. Xia, Y. Li, A phase field-based systematic multiscale topology optimization method for porous structures design, *J. Comput. Phys.* 466 (2022) 111383.
- [6] O. Sigmund, P.M. Clausen, Topology optimization using a mixed formulation: an alternative way to solve pressure load problems, *Comput. Methods Appl. Mech. Eng.* 196 (2007) 1874–1889.
- [7] Q. Yu, K. Wang, B. Xia, Y. Li, First and second order unconditionally energy stable schemes for topology optimization based on phase field method, *Appl. Math. Comput.* 405 (2021) 126267.
- [8] O. Sigmund, A 99 line topology optimization code written in Matlab, *Struct. Multidiscip. Optim.* 21 (2001) 120–127.
- [9] A. Pizzolatto, A. Sharma, K. Maute, A. Sciacovelli, V. Verda, Multi-scale topology optimization of multi-material structures with controllable geometric complexity: applications to heat transfer problems, *Comput. Methods Appl. Mech. Eng.* 357 (2019) 112552.
- [10] G. Delgado, M. Hamdaoui, Topology optimization of frequency dependent viscoelastic structures via a level-set method, *Appl. Math. Comput.* 347 (2019) 522–541.
- [11] Y. Liu, X. Wang, L. Wang, D. Liu, A modified leaky ReLU scheme (MLRS) for topology optimization with multiple materials, *Appl. Math. Comput.* 352 (2019) 188–204.
- [12] J.M. Guedes, N. Kikuchi, Preprocessing and postprocessing for materials based on the homogenization method with adaptive finite element methods, *Comput. Methods Appl. Mech. Eng.* 83 (1990) 143–198.
- [13] Y.M. Xie, G.P. Steven, Evolutionary Structural Optimization, Springer, Berlin, 1997.
- [14] M. Stolpe, K. Svanberg, An alternative interpolation scheme for minimum compliance optimization, *Struct. Multidiscip. Optim.* 22 (2001) 116–124.
- [15] M.P. Bendsøe, Optimal shape design as a material distribution problem, *Struct. Optim.* 1 (1989) 193–202.
- [16] A.R. Diaz, O. Sigmund, Checkerboard patterns in layout optimization, *Struct. Optim.* 10 (1995) 40–45.
- [17] O. Sigmund, K. Maute, Topology optimization approaches: a comparative review, *Struct. Multidiscip. Optim.* 48 (2013) 1031–1055.
- [18] Q. Xia, G. Sun, J. Kim, Y. Li, Multi-scale modeling and simulation of additive manufacturing based on fused deposition technique, *Phys. Fluids* 35 (2023) 034116.
- [19] Q. Xia, J. Yang, Y. Li, On the conservative phase-field method with the N-component incompressible flows, *Phys. Fluids* 35 (2023) 012120.
- [20] Y. Li, J. Kim, A comparison study of phase-field models for an immiscible binary mixture with surfactant, *Eur. Phys. J. B* 85 (2012) 340.
- [21] Y. Li, C. Luo, B. Xia, J. Kim, An efficient linear second order unconditionally stable direct discretization method for the phase-field crystal equation on surfaces, *Appl. Math. Model.* 67 (2019) 477–490.
- [22] C. Lee, D. Jeong, J. Shin, Y. Li, J. Kim, A fourth-order spatial accurate and practically stable compact scheme for the Cahn-Hilliard equation, *Physica A* 409 (2014) 17–28.
- [23] S. Osher, J.A. Sethian, Fronts propagating with curvature-dependent speed: algorithms based on Hamilton-Jacobi formulations, *J. Comput. Phys.* 79 (1988) 12–49.
- [24] J.A. Sethian, A. Wiegmann, Structural boundary design via level set and immersed interface methods, *J. Comput. Phys.* 163 (2000) 489–528.
- [25] A. Takezawa, S. Nishiwaki, M. Kitamura, Shape and topology optimization based on the phase field method and sensitivity analysis, *J. Comput. Phys.* 229 (2010) 2697–2718.
- [26] S. Osher, R. Fedkiw, Level Set Methods and Dynamic Implicit Surfaces, Springer-Verlag, New York, 2002.
- [27] S. Yamasaki, S. Nishiwaki, T. Yamada, K. Izui, M. Yoshimura, A structural optimization method based on the level set method using a new geometry-based re-initialization scheme, *Int. J. Numer. Methods Eng.* 83 (2010) 1580–1624.
- [28] P.H. Chiu, Y.T. Lin, A conservative phase field method for solving incompressible two-phase flows, *J. Comput. Phys.* 230 (2011) 185–204.
- [29] J.W. Cahn, J.E. Hilliard, Free energy of a nonuniform system. I. Interfacial free energy, *J. Comput. Phys.* 28 (1958) 258–267.
- [30] S.M. Allen, J.W. Cahn, A microscopic theory for antiphase boundary motion and its application to antiphase domain coarsening, *Acta Metall.* 27 (1979) 1085–1095.
- [31] S. Wang, R. Sekerka, A. Wheeler, B. Murray, S. Coriell, R. Braun, G. McFadden, Thermodynamically-consistent phase field models for solidification, *Physica D* 69 (1993) 189–200.
- [32] R. Kobayashi, Modeling and numerical simulations of dendritic crystal growth, *Physica D* 63 (1993) 410–423.
- [33] C. Lee, S. Yoon, J. Park, H. Kim, Y. Li, D. Jeong, S. Kim, S. Kwak, J. Kim, Phase-field computations of anisotropic ice crystal growth on a spherical surface, *Comput. Math. Appl.* 125 (2022) 25–33.
- [34] C. Miehe, M. Hofacker, F. Welschinger, A phase field model for rate-independent crack propagation: robust algorithmic implementation based on operator splits, *Comput. Methods Appl. Mech. Eng.* 199 (2010) 2765–2778.
- [35] Y. Li, J. Kim, Multiphase image segmentation using a phase-field model, *Comput. Math. Appl.* 62 (2011) 737–745.
- [36] B. Bourdin, A. Chambolle, Design-dependent loads in topology optimization, *ESAIM Control Optim. Calc. Var.* 9 (2003) 19–48.
- [37] B. Bourdin, A. Chambolle, The phase-field method in optimal design, in: IUTAM Symposium on Topological Design Optimization of Structures, Machines and Materials, vol. 137, 2006, pp. 207–215.
- [38] M. Wallin, M. Ristinmaa, Howard's algorithm in a phase-field topology optimization approach, *Int. J. Numer. Methods Eng.* 94 (2013) 43–59.
- [39] T. Takaki, J. Kato, Phase-field topology optimization model that removes the curvature effects, *Mech. Eng. J.* 4 (2017) 1–12.
- [40] Y. Sun, C. Beckermann, Sharp interface tracking using the phase-field equation, *J. Comput. Phys.* 220 (2007) 626–653.
- [41] N. Takada, J. Matsumoto, S. Matsumoto, A diffuse-interface tracking method for the numerical simulation of motions of a two-phase fluid on a solid surface, *J. Comput. Multiphase Flows* 6 (2014) 283–298.
- [42] L. Zhao, X. Bai, T. Li, J.J.R. Williams, Improved conservative level set method, *Int. J. Numer. Methods Fluids* 75 (2014) 575–590.
- [43] P.H. Chiu, A coupled phase field framework for solving incompressible two-phase flows, *J. Comput. Phys.* 392 (2019) 115–140.

- [44] J. Al-Salami, M.M. Kamra, C. Hu, A high order flux reconstruction interface capturing method with a phase field preconditioning procedure, *J. Comput. Phys.* 438 (2021) 488–510.
- [45] Y. Zhu, E. Sifakis, J. Teran, A. Brandt, An efficient multigrid method for the simulation of high-resolution elastic solids, *ACM Trans. Graph.* 29 (2010) 1–18.
- [46] S. Zhou, T. Rabczuk, X. Zhuang, Phase field modeling of quasi-static and dynamic crack propagation: COMSOL implementation and case studies, *Adv. Eng. Softw.* 122 (2018) 31–49.
- [47] B. Zhu, X. Zhang, S. Fatikow, Structural topology and shape optimization using a level set method with distance-suppression scheme, *Comput. Methods Appl. Mech. Eng.* 283 (2015) 1214–1239.
- [48] S. Shojaei, A. Mohaghegh, A. Haeri, Piecewise constant level set method based finite element analysis for structural topology optimization using phase field method, *Int. J. Optim. Civil. Eng.* 5 (2015) 389–407.
- [49] Y. Li, Y. Choi, J. Kim, Computationally efficient adaptive time step method for the Cahn-Hilliard equation, *Comput. Math. Appl.* 73 (2017) 1855–1864.
- [50] Y. Li, D. Jeong, H. Kim, C. Lee, J. Kim, Comparison study on the different dynamics between the Allen-Cahn and the Cahn-Hilliard equations, *Comput. Math. Appl.* 77 (2019) 311–322.
- [51] J. Long, C. Luo, Q. Yu, Y. Li, An unconditional stable compact fourth-order finite difference scheme for three dimensional Allen-Cahn equation, *Comput. Math. Appl.* 77 (2019) 1042–1054.
- [52] Y. Li, S. Lan, X. Liu, B. Lu, L. Wang, An efficient volume repairing method by using a modified Allen-Cahn equation, *Pattern Recognit.* 107 (2020) 107478.
- [53] N. Shervani-Tabar, O.V. Vasilyev, Stabilized conservative level set method, *J. Comput. Phys.* 375 (2018) 1033–1044.
- [54] Z. Jibben, M. Herrmann, An arbitrary-order Runge-Kutta discontinuous Galerkin approach to reinitialization for banded conservative level sets, *J. Comput. Phys.* 349 (2017) 453–473.
- [55] K. Glasner, Nonlinear preconditioning for diffuse interfaces, *J. Comput. Phys.* 174 (2001) 695–711.
- [56] Y. Li, J.-I. Choi, J. Kim, A phase-field fluid modeling and computation with interfacial profile correction term, *Commun. Nonlinear Sci. Numer. Simul.* 30 (2016) 84–100.
- [57] Y. Luo, J. Bao, A material-field series-expansion method for topology optimization of continuum structures, *Comput. Struct.* 225 (2019) 106122.
- [58] Y. Luo, J. Xing, Z. Kang, Topology optimization using material-field series expansion and Kriging-based algorithm: an effective non-gradient method, *Comput. Methods Appl. Mech. Eng.* 364 (2020) 112966.
- [59] S. Lee, H. Kim, Q.X. Lieu, J. Lee, CNN-based image recognition for topology optimization, *Knowl.-Based Syst.* 198 (2020) 105887.
- [60] J. Liu, J. Yan, H. Yu, Stress-constrained topology optimization for material extrusion polymer additive manufacturing, *J. Comput. Des. Eng.* 8 (2021) 979–993.
- [61] Y. Li, J. Choi, J. Kim, Multi-component Cahn-Hilliard system with different boundary conditions in complex domains, *J. Comput. Phys.* 323 (2016) 1–16.
- [62] Y. Li, D. Jeong, J. Shin, J. Kim, A conservative numerical method for the Cahn-Hilliard equation with Dirichlet boundary conditions in complex domains, *Comput. Math. Appl.* 65 (2013) 102–115.